

Nanoscale Control of One-Dimensional Confined States in Strongly Correlated Homojunctions

Quanzhen Zhang,[#] Yu Zhang,^{*,#} Yanhui Hou, Runzhang Xu, Lianguang Jia, Zeping Huang, Xiaoyu Hao, Jiadong Zhou, Teng Zhang, Liwei Liu, Yong Xu, Hong-Jun Gao, and Yeliang Wang*



Cite This: *Nano Lett.* 2022, 22, 1190–1197



Read Online

ACCESS |



Metrics & More



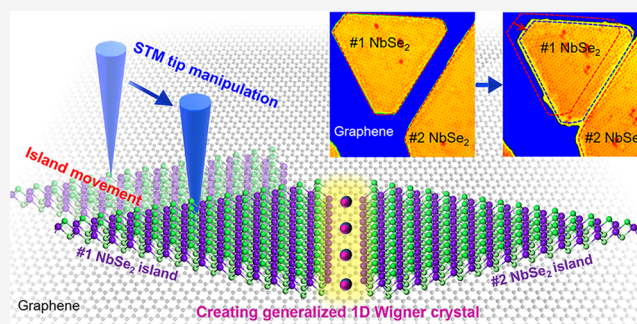
Article Recommendations



Supporting Information

ABSTRACT: Construction of lateral junctions is essential to generate one-dimensional (1D) confined potentials that can effectively trap quasiparticles. A series of remarkable electronic phases in one dimension, such as Wigner crystallization, are expected to be realized in such junctions. Here, we demonstrate that we can precisely tune the 1D-confined potential with an in situ manipulation technique, thus providing a dynamic way to modify the correlated electronic states at the junctions. We confirm the existence of 1D-confined potential at the homojunction of two single-layer 1T-NbSe₂ islands. Such potential is structurally sensitive and shows a nonmonotonic function of their interspacing. Moreover, there is a change of electronic properties from the correlated insulator to the generalized 1D Wigner crystallization while the confinement becomes strong. Our findings not only establish the capability to fabricate structures with dynamically tunable properties, but also pave the way toward more exotic correlated systems in low dimensions.

KEYWORDS: 1D-confined potential, homojunction, generalized 1D Wigner crystallization, STM manipulation, correlated insulator



Two-dimensional (2D) materials have drawn intense attention because they can be manipulated to form different electronic structures, which gives rise to a variety of strongly correlated physical properties once the long-range Coulomb interaction exceeds the kinetic energy of electrons.¹ Typically, the Mott insulator, charge-density-wave (CDW) phase, superconductivity, Wigner crystallization, and Chern insulator have been reported in atomically thin films of pristine transition-metal dichalcogenides (TMDs)^{2–12} and their moiré superlattices,^{13–15} as well as the magic-angle twisted bilayer graphene.^{16–20}

Moreover, the construction of one-dimensional (1D) homostructures and heterostructures based on 2D TMDs has attracted widespread attention recently. Among them, the in-plane 1D structures that consist of atomically thin TMDs with strongly correlated electrons are especially important, as they hold potential for exploring 1D-correlated electronic properties.^{21–29} Note that the depth and width of 1D-confined electron potentials are supposed to be tuned by changing the interspacing of the lateral structures. Therefore, the in-plane lateral structures provide unique and brand-new platforms to systemically study the 1D-correlated electron behaviors at the junction. Recently, the 1D homojunctions and heterojunctions are expected to spontaneously form using a molecular beam epitaxy (MBE) method.^{30,31} However, to the best of our knowledge, the technique for controllable fabrication of lateral

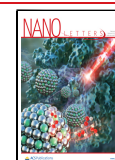
structures in situ with clean and atomically sharp junctions has been challenging up until now.

In the current work, we focus on the fabrications and tunable properties of lateral homojunctions composed of two isolated single-layer 1T-NbSe₂ (STNS) islands supported on the bilayer graphene (BLG)/SiC(0001) substrate. We develop an in situ scanning tunneling microscopy (STM) tip manipulation technique, which can controllably drive the STNS islands to slide on BLG in translational and rotational motions with atomic precision. By precisely tune the interspacing of two STNS islands, we successfully realize three different regimes of 1D electron confinement, that is, non-confined, weakly confined, and strongly confined regimes, at the STNS-based homojunctions. In particular, at the strongly confined regime, the signatures of 1D-generalized Wigner crystallization is visualized at the homojunction in real space. In short, our results achieve dynamic tunability of the homostructures and correlated electronic properties in 1D-

Received: November 11, 2021

Revised: January 11, 2022

Published: January 19, 2022



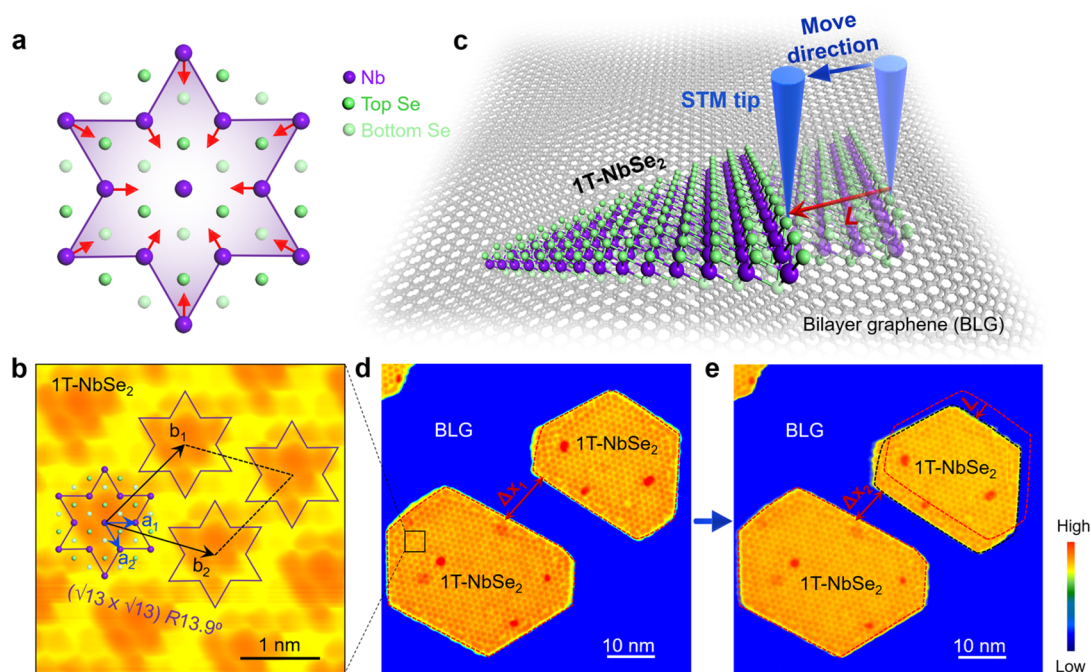


Figure 1. Translational motion of SL 1T-NbSe₂ (STNS) islands on bilayer graphene (BLG) using an in situ STM manipulation technique. (a) Schematic of the star-of-David (SOD) cluster in STNS viewed from the top. Nb, top Se, and bottom Se atoms are displayed by purple, green, and light green spheres, respectively. In each SOD cluster, 12 surrounding Nb atoms contract toward one central Nb atom, as indicated by red arrows. (b) Zoomed-in atomic-resolution STM image of the STNS on BLG ($V_s = -1$ V, $I_t = 500$ pA), as marked by the black dashed rectangle in panel (d). The top Se atoms in each SOD cluster dominate the STM images as a triangular bright protrusion. a_1/a_2 and b_1/b_2 represent the basis vectors of (1×1) atomic lattices and $(\sqrt{13} \times \sqrt{13})$ R13.9° CDW lattices, respectively. (c) Schematic description of STM manipulation technique. The STM tip moves along the preset trajectory perpendicular to the edge of STNS island, as marked by the blue arrow. When the STM tip encounters the STNS island, the island begins to slide on BLG along the direction marked by the red arrow for the distance of L . (d,e) Experimental realization of STNS islands sliding on BLG in a translational motion. Panels (d) and (e) are the representative STM images before and after the manipulation, respectively ($V_s = -1$ V, $I_t = 10$ pA). The STNS island in the upper right corner translates on BLG for a distance L .

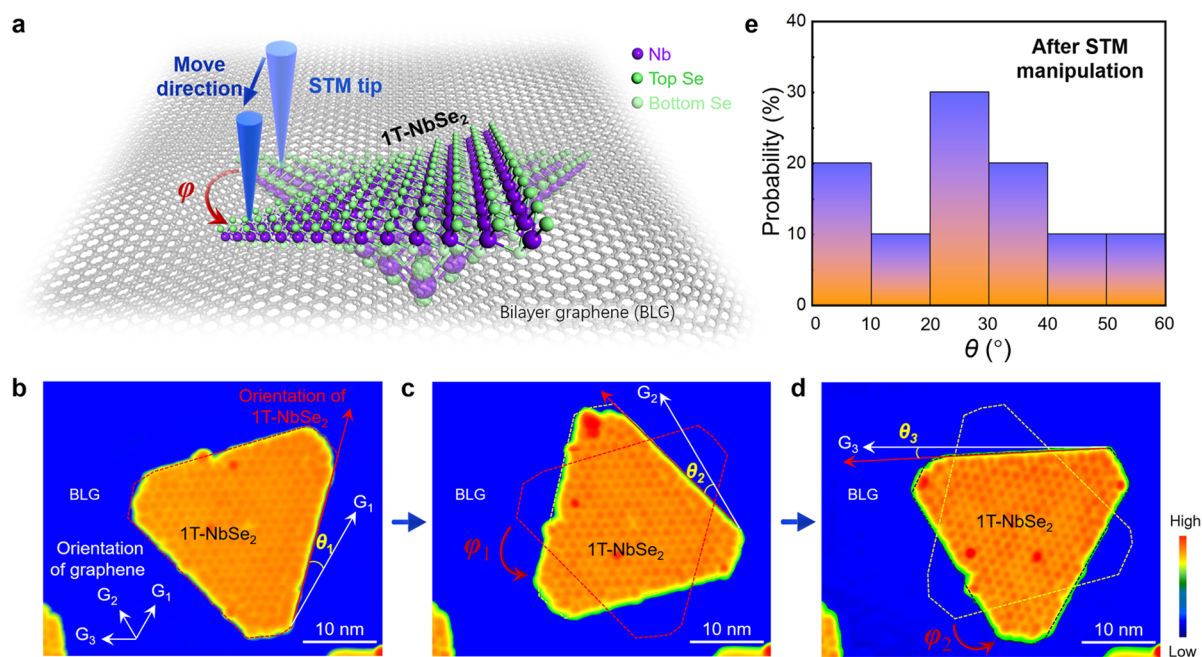


Figure 2. Rotational motion of STNS islands on BLG using an in situ STM manipulation technique. (a) Schematic description of STM manipulation technique. The STM tip moves along the preset trajectory across the corner of a STNS island, as marked by the blue arrow. When the STM tip encounters the STNS island, the island begins to rotate with an angle of φ . (b–d) Three representative STM images of an STNS island on BLG with three different orientations after the STM-tip manipulation ($V_s = -1.5$ V, $I_t = 10$ pA). The red arrow indicates the lattice orientation of the island, and the white arrows indicate the three equivalent orientations of BLG. (e) Statistical graph of probability as a function of the twist angle θ between STNS and BLG.

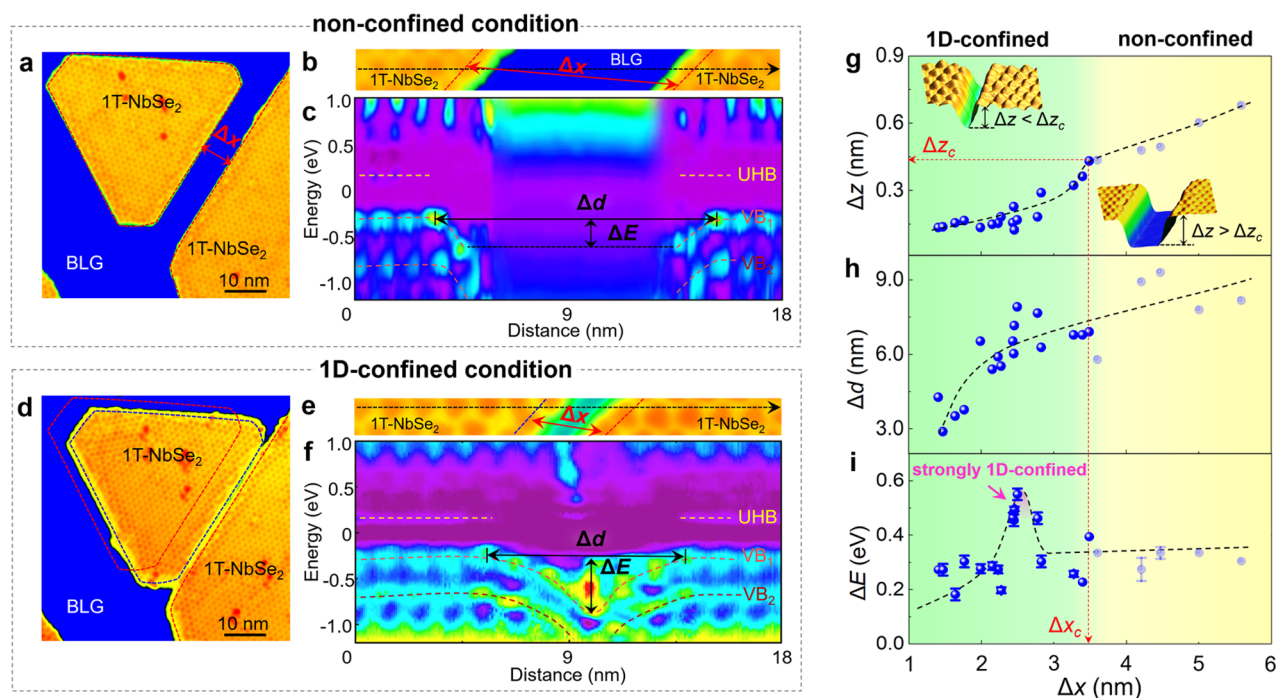


Figure 3. Tunable 1D quantum confinement of correlated electrons at the STNS-based homojunction. (a,d) Representative STM images of two STNS islands on BLG with different interspacing via a STM-tip manipulation technique ($V_s = -1.5$ V, $I_t = 10$ pA). (b,e) Zoomed-in STM images of the STNS-based homojunctions in panels (a) and (d), respectively. Δx represents the interspacing between the center of two nearest neighbor SOD clusters from the two STNS islands. (c,f) Spatially resolved dI/dV spectra measured across the STNS-based homojunction that marked by the black arrows in panels (b) and (e), respectively. Δd and ΔE represent the width and depth of the 1D-confined electron potential. Specifically, ΔE is defined as the bending energy of the VB_1 at the edge of STNS for the non-confined condition or the bending energy of the VB_1 at the homojunctions for the weakly or strongly confined conditions. Δd represents the spatial distance between the positions where the VB_1 of the two adjacent islands starts to bend. (g–i) Δz , Δd , and ΔE as a function of Δx , respectively. Δz is the apparent depth of the STNS-based homojunction that exhibited in the STM images. The critical value of Δz , $\Delta z_c \approx 0.44$ nm, is the boundary between the regions of 1D-confined ($\Delta z < \Delta z_c$) and non-confined ($\Delta z > \Delta z_c$) correlated electrons.

confined systems, paving the way toward next-generation electronic nanodevices.

RESULTS AND DISCUSSION

In our experiments, we directly fabricate STNS islands on BLG/SiC(0001) using a MBE method in a Se-rich atmosphere, as we reported previously.^{32–35} The atomic lattice of STNS usually experiences a CDW transition at low temperature, resulting in an ordered ($\sqrt{13} \times \sqrt{13}$) triangular superlattice with star-of-David (SOD) motifs. In each SOD, 12 surrounding Nb atoms contract toward one central Nb atom,^{5,32,33} as depicted in Figure 1a,b. Moreover, the edges of STNS islands usually exhibit well-ordered zigzag configurations, according to our atomic-resolution STM image shown in Figure S1.

To achieve the tunable STNS-based 1D homojunction with atomic precision, we explore two mechanical manipulation techniques to slide the as-grown STNS islands on BLG via a STM tip at the liquid helium temperature. One is schematically shown in Figure 1c, in which the island slides on BLG in a translational motion. Briefly, we first bring the STM tip close to BLG substrate with the tunneling current of 1 nA and the bias voltage of -0.1 V, and then we move the STM tip along the preset trajectory (blue arrow in Figure 1c) to push the STNS island from an edge, thus the island can translate on BLG in an expected direction. Simultaneously, the STM-tip imaging provides a real-time measurement of the manipulating consequence. Figure 1d,e shows the representative STM

images of two STNS islands on BLG before and after our STM-tip manipulation. As we can see, the translational motion of the STNS island can be clearly captured. Such a phenomenon can be attributed to the low mechanical friction between STNS and BLG.^{36–39}

The other STM-tip manipulation technique is schematically illustrated in Figure 2a. For the as-grown samples, the STNS lattices usually align to the underlying BLG lattices, which can be deduced from large-scale STM images in Figure S2. When the STM tip is driven to move across one corner of the STNS island under the condition of a small tip–BLG distance (the trajectory of the STM tip is marked by the blue arrow in Figure 2a), the STNS island is expected to rotate on the BLG. Extensive experiments have verified that the moving velocity of the STM tip should be slower than 1 nm/s to guarantee the island rotates in situ.

Figure 2b–d shows three representative STM images of a STNS island on the BLG after the STM-tip manipulation. The lattice orientations of STNS and BLG, marked by red and white arrows, respectively, are obviously distinct for these three statuses. To further investigate the preferred orientation, numerous manipulations of rotating STNS islands on BLG, accompanied by the real-time STM imaging, are systematically performed. Here, we summarize the probability as a function of the twisted angles θ between STNS and BLG after the manipulation in Figure 2e. Surprisingly, there is no obvious orientation preference, implying no energetically favorable orientation. Such a result, at first glance, is counterintuitive, but

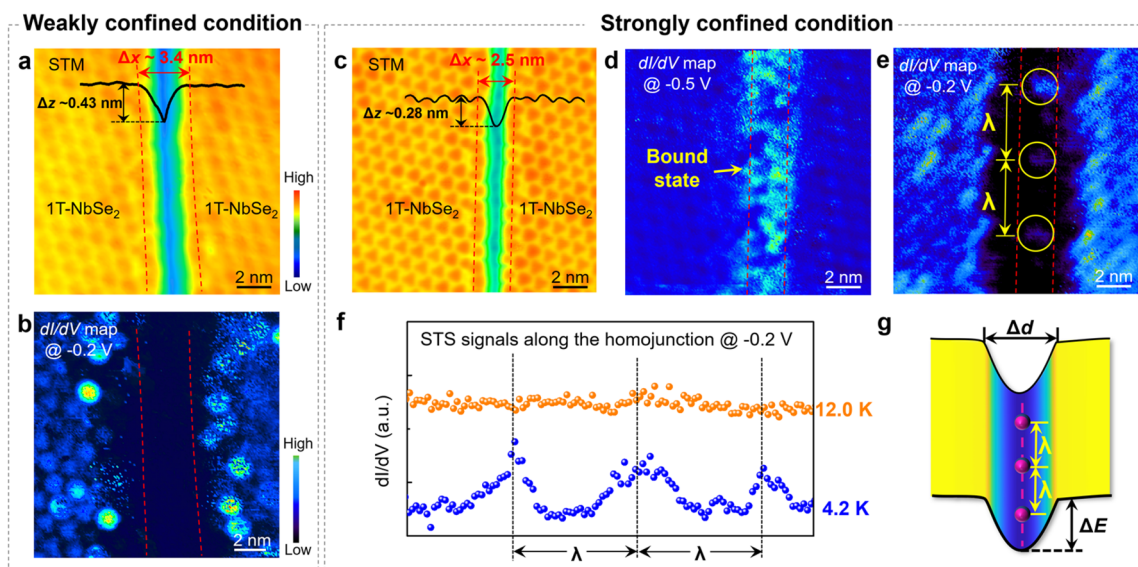


Figure 4. Electronic properties at the STNS-based homojunctions. (a) Topographic STM images of two STNS islands with their interspacing $\Delta x \approx 3.4$ nm ($V_s = -1$ V, $I_t = 10$ pA). (b) dI/dV maps recorded in the region of panel (a) at the bias of -0.2 V. (c) Topographic STM images of two STNS islands with their interspacing $\Delta x \approx 2.5$ nm ($V_s = -1$ V, $I_t = 10$ pA). (d) dI/dV maps recorded in the region of panel (c) at the bias of -0.5 V. The bound state can be observed at the homojunction. (e) dI/dV maps recorded in the region of panel (c) at the bias of -0.2 V. The 1D Wigner crystallization with the superlattice constant $\lambda \approx 5$ nm is shown at the homojunction. (f) Typical STS signals along the STNS-based homojunctions at the bias of -0.2 V with different sample temperatures of 4.2 and 12.0 K. (g) Schematic of 1D Wigner crystallization at the 1D-confined correlated system.

can be well-understood with the picture that the large lattice mismatch between STNS and graphene results in a negligible contribution to the interface friction.³⁹ Therefore, STNS islands can be stable on BLG at arbitrary twisted angles during the STM-tip manipulation.

Such STM-tip manipulation processes have been successfully applied to tens of STNS islands on BLG, with their sizes varying from 300 to 1900 nm². Figure 3a,d shows representative STM images of two STNS islands on BLG using a STM-tip manipulation technique. The zoomed-in STM images of the homojunctions are given in Figure 3b,e. For both conditions, the adjacent edges of two STNS islands are parallel to each other, with their interspacing Δx of about 8.3 and 2.5 nm. Here, we define Δx as the spatial distance between the center of two nearest neighbor SOD clusters from different 1T-NbSe₂ islands, as clearly marked in Figure 3b,e.

In the following, we will focus on the electronic properties within the 1D-confined electron potential that is generated by STNS-based homojunctions. Figure 3c,f exhibits the spatially resolved scanning tunneling spectroscopy (STS) spectra recorded across the homojunctions that are marked by the black arrows in Figure 3b,e, respectively (more data and analysis are given in Figures S3–S5). In the bulk STNS, the STS spectra exhibit a charge-transfer insulating state, with the upper Hubbard band (UHB) located at the energy of about 0.16 eV and the lower Hubbard band (LHB) hybridizing with the valence band (VB). In addition, the density of states (DOS) peaks at the energies of about -0.29 and -0.75 eV are attributed to the VB₁ and VB₂, respectively. These results are consistent with previous STS studies.^{9,10}

The STS spectra recorded around the STNS-based homojunctions exhibit significant structural and spatially dependent features. When the two STNS islands are away from each other, for example, $\Delta x \approx 8.3$ nm (Figure 3a–c), the electrons at the two adjacent edges of these two islands are

decoupled, leaving each edge at the homojunction behaving as an isolated STNS edge. Therefore, we can acquire the intrinsic electronic features of both the isolated edge state in STNS and the BLG within the two edges. As shown in Figure 3c, we find there are two significant features at an isolated STNS edge. First, both the VB₁ and VB₂ exhibit an effective downward band bending at the edge of STNS, with a bending energy of $\Delta E \approx 0.29$ eV. Second, the signal of UHB becomes gradually weak while approaching the edge, which can be attributed to the different electronic fillings of the flat band at the edge.

Surprisingly, when the two STNS islands approach each other with a small separation, $\Delta x \approx 2.5$ nm (Figure 3d–f), the spatially resolved STS spectra acquired around the STNS-based homojunction change dramatically, as shown in Figure 3f. Within the STNS-based homojunction, there is almost no signal of the metallic state that is attributed to the BLG substrate, illustrating that the two adjacent edges at the homojunction are electronically coupled. One of most intriguing features exhibited in Figure 3f is that the band bending effect in the STNS-based homojunction is much more significant, with the downward bending energy reaching $\Delta E \approx 0.57$ eV, which is 2 times larger than that in an isolated STNS edge. Therefore, the 1D confinement of correlated electrons is achieved at the STNS-based homojunction. More details about the exotic DOS peaks at the homojunction will be discussed later.

To systemically study the correlated electronic behavior at the STNS-based homojunctions, we measure the structural and electronic characteristics of the homojunctions as a function of the interspacing Δx between two adjacent islands, as summarized in Figure 3g–i (Figure S6 for more data). On the one hand, the depth of STNS-based homojunctions Δz exhibited in the profile line of the STM image varies with Δx (the apparent height of STNS in STM images is about 0.7 nm). Considering that both the electronic states and

topographic features have contributions to the STM images, the measured depth $\Delta z < 0.7$ nm at the homojunction is supposed to result from the orbital coupling of the two adjacent edges. Based on the STS spectra, we define the critical depth of the homojunction $\Delta z_c \approx 0.44$ nm at $\Delta x_c \approx 3.6$ nm, as marked in Figure 3g. When $\Delta z > \Delta z_c$, the metallic states can be detected within the homojunction, which are attributed to the underlying graphene sheet. When $\Delta z < \Delta z_c$, the metallic states of graphene are completely screened, implying the correlated electrons at the edges of STNS are well-confined in the 1D homojunction.

On the other hand, both the width and depth of the 1D-confined electron potential wells that consist of STNS-based homojunctions exhibit significant variation with Δx (Figure 3h,i). For $\Delta x < \Delta x_c$, although the width of the 1D-confined electron potential well Δd decreases with decreasing Δx , its depth is a nonmonotonic function of Δx , as shown in Figure 3i. Specifically, as Δx decreases, the 1D-confining capability of the STNS-based homojunctions first gets stronger and then becomes weaker. When $\Delta x \approx 2.5$ nm, the depth of 1D-confined electron potential well reaches a maximum $\Delta E \approx 0.57$ eV. Although we could not obtain a theoretical explanation for such a nonmonotonic feature so far, it can be well-captured from the point of view of the limit that the confined potential should vanish when Δx is close to the superlattice constant of the SOD motifs of about 1.2 nm. Therefore, the non-monotonic relation between ΔE and Δx is expected.

Based on our experimental phenomena, the behavior of correlated electrons confined into the STNS-based homojunctions can be divided into three conditions, that is, non-confined ($\Delta x > \Delta x_c$), weakly confined ($\Delta x < \Delta x_c$ and $\Delta E < 0.50$ eV), and strongly confined ($\Delta x < \Delta x_c$ and $\Delta E > 0.50$ eV) conditions. To further explore the 1D electronic behaviors, we performed the measurements of dI/dV maps at STNS-based homojunctions, which directly reflect the spatial distribution of the local DOS at the recorded energies. For the non-confined condition ($\Delta x > \Delta x_c$), a metallic state is well-captured in the interstice of two STNS islands (Figure S7), which is attributed to the graphene substrate. For the weakly confined condition ($\Delta x < \Delta x_c$ and $\Delta E < 0.50$ eV), neither the graphene-related metallic state nor the 1D-confined state is observed within the homojunctions, although there is an electron potential well with the depth $\Delta E \approx 0.25$ eV, as shown in Figure 4a,b.

Importantly, for the strongly confined condition ($\Delta x < \Delta x_c$ and $\Delta E > 0.50$ eV), the electrons exhibit quite distinct behaviors. Figure 4c–e shows a representative STM image of STNS-based homojunctions with $\Delta x \approx 2.5$ nm and the corresponding dI/dV maps. At the energy of -0.5 eV, an obvious 1D electronic pattern (Figure 4d) can be observed along the confined electron potential well (as described in Figure 3f), which can be attributed to the bound state of the STNS-based homojunctions.

It is worth noting that, at the energy of -0.2 eV, the electrons within the potential well prefer to crystallize into a periodic arrangement with the wavelength $\lambda \approx 5$ nm, as shown in Figure 4e. Here, we can rule out the influence of the edge states in STNS because the edge states should appear at all the STNS edges, regardless of the confined conditions. In addition, our high-resolution STM images in Figure 4c can help us rule out any possible influence of the defects or impurities. Similar observations of electron crystallized arrangements are also obtained at other strongly confined regimes with different STM tips, which helps us rule out any possible artifacts.

Moreover, we carry out the spatially resolved STS measurements along the STNS-based homojunction for the strongly confined condition ($\Delta x < \Delta x_c$ and $\Delta E > 0.50$ eV) at different sample temperatures. Figure 4f shows the intensity of STS signals (i.e., DOS of electrons) along the STNS-based homojunction at the energy of -0.2 eV with the sample temperatures of 4.2 and 12.0 K. We can clearly observe that the periodicity of the crystallization completely disappears at 12.0 K.

Such a temperature-dependent crystallization signature of electrons in the STNS-based homojunction is reminiscent of the 1D-generalized Wigner crystallization.⁴⁰ In fact, Wigner crystallization was theoretically predicted by Wigner in 1934⁴¹ and has been experimentally achieved in van der Waals structures in the last 2 years.^{18,19,42–44} Based on previous studies, the realization of the Wigner crystal requires three essential conditions, that is, strong electronic interactions, low carrier densities, and no disorders, which can be more easily satisfied simultaneously in low-dimensional systems.^{18,42–46} Moreover, the Wigner crystal is extremely sensitive to the temperature, according to previous studies.^{13,44}

For electrons in our STNS case, the long-range Coulomb interaction E_U is strong enough to overcome the kinetic energy E_K , resulting in an insulating state at the Fermi energy. In such case, an extremely low density of charge n , together with a large electron effective mass m^* , can be realized in STNS.^{9,10} When these correlated electrons are strongly confined into one dimension, the criterion of Wigner crystallization, which can be estimated as $na^* < 1$ ($a^* = \epsilon \hbar^2 / (m^* e^2)$ is the effective Bohr radius, ϵ is the dielectric constant, and \hbar is Planck's constant), is satisfied.^{18,41–46} Therefore, the STNS-based 1D homojunctions are expected to provide a natural platform for realizing the 1D-generalized Wigner crystal, as schematically shown in Figure 4g. Although we could not provide more experimental evidence of the Wigner crystal state in our samples so far, we indeed observe the signatures of 1D-generalized Wigner crystallization. A more in-depth physical mechanism needs to be further explored. Because the 1D Wigner crystallization is anticipated to display a rich landscape of novel spin and magnetic properties,⁴⁰ it is powerful for the development of quantum information.

CONCLUSIONS

In conclusion, we have developed an in situ STM manipulation technique to realize the translation and rotation of TMD islands on demand. By precisely tuning the interspacing of two STNS islands, we successfully realized the construction of desirable lateral homostructures with controllable width. Such artificial nanostructures constructed at atomic scale provide a novel platform to explore emergent electronic properties. We find there exists tunable 1D-confined electron potentials at the STNS-based homojunctions, which dominate the electronic characteristics varying from a correlated insulator to 1D-generalized Wigner crystallization. Our results provide a distinctive opportunity for demonstrating innovative electronic properties and designing novel quantum nanodevices.

EXPERIMENTAL METHOD

The sample preparation and STM measurements were performed with a custom-designed Unisoku STM system (USM-1300). First, the bilayer graphene was obtained by thermal decomposition of 4H-SiC(0001) at 1200 °C for 45

min. Next, the single-layer 2H-NbSe₂ islands were epitaxially grown on the BLG/SiC(0001) substrate by evaporating Nb and Se from an electron beam evaporator and a Knudsen cell evaporator, respectively. The flux ratio of Nb and Se is approximately 1:20 to guarantee a rich Se environment. The growth rate of 2H-NbSe₂ is 0.002 ML/min. The BLG/SiC(0001) substrate was maintained at 500 °C during the growth, followed by a postannealing process at 400 °C for 20 min.

The STM and STS measurements were performed in the ultra-high-vacuum chamber ($\sim 10^{-11}$ Torr) with constant-current scanning mode. The experiments were acquired at the temperature of 4.2 K. An electrochemically etched tungsten tip was used as the STM probe, which was calibrated by using a standard graphene lattice, a Si (111)-(7 × 7) lattice, and a Ag(111) surface. The STS measurements were taken by a standard lock-in technique with the bias modulation of 5 mV at 973 Hz.

■ ASSOCIATED CONTENT

SI Supporting Information

The Supporting Information is available free of charge at <https://pubs.acs.org/doi/10.1021/acs.nanolett.1c04363>.

Typical STM image of as-grown STNS islands on BLG; spatially resolved dI/dV spectra measured across the STNS-based homojunctions; electronic properties at the STNS-based homojunction under the non-confined condition (PDF)

■ AUTHOR INFORMATION

Corresponding Authors

Yu Zhang – School of Integrated Circuits and Electronics, MIIT Key Laboratory for Low-Dimensional Quantum Structure and Devices and Advanced Research Institute of Multidisciplinary Science, Beijing Institute of Technology, Beijing 100081, China; orcid.org/0000-0003-1290-7980; Email: yzhang@bit.edu.cn

Yeliang Wang – School of Integrated Circuits and Electronics, MIIT Key Laboratory for Low-Dimensional Quantum Structure and Devices, Beijing Institute of Technology, Beijing 100081, China; orcid.org/0000-0002-8896-0748; Email: yeliang.wang@bit.edu.cn

Authors

Quanzhen Zhang – School of Integrated Circuits and Electronics, MIIT Key Laboratory for Low-Dimensional Quantum Structure and Devices, Beijing Institute of Technology, Beijing 100081, China; orcid.org/0000-0003-3423-5863

Yanhui Hou – School of Integrated Circuits and Electronics, MIIT Key Laboratory for Low-Dimensional Quantum Structure and Devices, Beijing Institute of Technology, Beijing 100081, China

Runzhang Xu – State Key Laboratory of Low Dimensional Quantum Physics and Department of Physics, Tsinghua University, Beijing 100084, China

Liangguang Jia – School of Integrated Circuits and Electronics, MIIT Key Laboratory for Low-Dimensional Quantum Structure and Devices, Beijing Institute of Technology, Beijing 100081, China

Zeping Huang – School of Integrated Circuits and Electronics, MIIT Key Laboratory for Low-Dimensional Quantum

Structure and Devices, Beijing Institute of Technology, Beijing 100081, China

Xiaoyu Hao – School of Integrated Circuits and Electronics, MIIT Key Laboratory for Low-Dimensional Quantum Structure and Devices, Beijing Institute of Technology, Beijing 100081, China

Jiadong Zhou – School of Integrated Circuits and Electronics, MIIT Key Laboratory for Low-Dimensional Quantum Structure and Devices, Beijing Institute of Technology, Beijing 100081, China; orcid.org/0000-0001-5268-2136

Teng Zhang – School of Integrated Circuits and Electronics, MIIT Key Laboratory for Low-Dimensional Quantum Structure and Devices, Beijing Institute of Technology, Beijing 100081, China; orcid.org/0000-0001-8739-7773

Liwei Liu – School of Integrated Circuits and Electronics, MIIT Key Laboratory for Low-Dimensional Quantum Structure and Devices, Beijing Institute of Technology, Beijing 100081, China; orcid.org/0000-0001-5884-7333

Yong Xu – State Key Laboratory of Low Dimensional Quantum Physics and Department of Physics, Tsinghua University, Beijing 100084, China; orcid.org/0000-0002-4844-2460

Hong-Jun Gao – Institute of Physics, Chinese Academy of Sciences, Beijing 100190, China; orcid.org/0000-0002-6766-0623

Complete contact information is available at:

<https://pubs.acs.org/doi/10.1021/acs.nanolett.1c04363>

Author Contributions

*Q.Z. and Y.Z. contributed equally to this work.

Notes

The authors declare no competing financial interest.

■ ACKNOWLEDGMENTS

We thank the National Natural Science Foundation of China (Nos. 92163206, 61725107, 61971035, 61901038, and 62101037), National Key Research and Development Program of China (2019YFA0308000, 2020YFA0308800, 2021YFA1400100), Beijing Natural Science Foundation (Nos. Z190006 and 4192054), and China Postdoctoral Science Foundation (2020M680382, 2021M700407) for the financial support.

■ REFERENCES

- (1) Lieb, E. H. Two theorems on the Hubbard model. *Phys. Rev. Lett.* **1989**, *62*, 1201–1204.
- (2) Sipos, B.; Kusmartseva, A. F.; Akrap, A.; Berger, H.; Forro, L.; Tutis, E. From Mott state to superconductivity in 1T-TaS₂. *Nat. Mater.* **2008**, *7*, 960–965.
- (3) Xi, X.; Zhao, L.; Wang, Z.; Berger, H.; Forró, L.; Shan, J.; Mak, K. F. Strongly enhanced charge-density-wave order in monolayer NbSe₂. *Nat. Nanotechnol.* **2015**, *10*, 765–769.
- (4) Yu, Y.; Yang, F.; Lu, X. F.; Yan, Y. J.; Cho, Y. H.; Ma, L.; Niu, X.; Kim, S.; Son, Y.; Feng, D.; Li, S.; Cheong, S. W.; Chen, X. H.; Zhang, Y. Gate-tunable phase transitions in thin flakes of 1T-TaS₂. *Nat. Nanotechnol.* **2015**, *10*, 270–276.
- (5) Nakata, Y.; Sugawara, K.; Shimizu, R.; Okada, Y.; Han, P.; Hitosugi, T.; Ueno, K.; Sato, T.; Takahashi, T. Monolayer 1T-NbSe₂ as a Mott insulator. *NPG Asia Mater.* **2016**, *8*, e321.
- (6) Calandra, M. Phonon-assisted magnetic Mott-insulating state in the charge density wave phase of single-layer 1T-NbSe₂. *Phys. Rev. Lett.* **2018**, *121*, 026401.
- (7) Chen, Y.; Ruan, W.; Wu, M.; Tang, S.; Ryu, H.; Tsai, H.; Lee, R.; Kahn, S.; Liou, F.; Jia, C.; Albertini, O. R.; Xiong, H.; Jia, T.; Liu, Z.

- Sobota, J. A.; Liu, A. Y.; Moore, J. E.; Shen, Z.; Louie, S. G.; Mo, S.; Crommie, M. F. Strong correlations and orbital texture in single-layer 1T-TaSe₂. *Nat. Phys.* **2020**, *16*, 218–224.
- (8) Ruan, W.; Chen, Y.; Tang, S.; Hwang, J.; Tsai, H.; Lee, R. L.; Wu, M.; Ryu, H.; Kahn, S.; Liou, F.; Jia, C.; Aikawa, A.; Hwang, C.; Wang, F.; Choi, Y.; Louie, S. G.; Lee, P. A.; Shen, Z.; Mo, S.; Crommie, M. F. Evidence for quantum spin liquid behaviour in single-layer 1T-TaSe₂ from scanning tunnelling microscopy. *Nat. Phys.* **2021**, *17*, 1154–1161.
- (9) Liu, Z.-Y.; Qiao, S.; Huang, B.; Tang, Q.-Y.; Ling, Z.-H.; Zhang, W.-H.; Xia, H.-N.; Liao, X.; Shi, H.; Mao, W.-H.; Zhu, G.-L.; Lu, J.-T.; Fu, Y.-S. Charge transfer gap tuning via structural distortion in monolayer 1T-NbSe₂. *Nano Lett.* **2021**, *21*, 7005–7011.
- (10) Liu, M.; Leveillee, J.; Lu, S.; Yu, J.; Kim, H.; Tian, C.; Shi, Y.; Lai, K.; Zhang, C.; Giustino, F.; Shih, C.-K. Monolayer 1T-NbSe₂ as a 2D correlated magnetic insulator. *Sci. Adv.* **2021**, *7*, No. eabi6339.
- (11) Tsen, A. W.; Hovden, R.; Wang, D.; Kim, Y. D.; Okamoto, J.; Spoth, K. A.; Liu, Y.; Lu, W.; Sun, Y.; Hone, J. C.; Kourkoutis, L. F.; Kim, P.; Pasupathy, A. N. Structure and control of charge density waves in two-dimensional 1T-TaS₂. *P. Natl. Acad. Sci.* **2015**, *112*, 15054–15059.
- (12) Wang, K.; De Greve, K.; Jauregui, L. A.; Sushko, A.; High, A.; Zhou, Y.; Scuri, G.; Taniguchi, T.; Watanabe, K.; Lukin, M. D.; Park, H.; Kim, P. Electrical control of charged carriers and excitons in atomically thin materials. *Nat. Nanotechnol.* **2018**, *13*, 128–132.
- (13) Regan, E. C.; Wang, D.; Jin, C.; Bakti Utama, M. I.; Gao, B.; Wei, X.; Zhao, S.; Zhao, W.; Zhang, Z.; Yumigeta, K.; Blei, M.; Carlstrom, J. D.; Watanabe, K.; Taniguchi, T.; Tongay, S.; Crommie, M.; Zettl, A.; Wang, F. Mott and generalized Wigner crystal states in WSe₂/WS₂ moiré superlattices. *Nature* **2020**, *579*, 359–363.
- (14) Li, H.; Li, S.; Regan, E. C.; Wang, D.; Zhao, W.; Kahn, S.; Yumigeta, K.; Blei, M.; Taniguchi, T.; Watanabe, K.; Tongay, S.; Zettl, A.; Crommie, M. F.; Wang, F. Imaging two-dimensional generalized Wigner crystals. *Nature* **2021**, *597*, 650–654.
- (15) Jin, C.; Tao, Z.; Li, T.; Xu, Y.; Tang, Y.; Zhu, J.; Liu, S.; Watanabe, K.; Taniguchi, T.; Hone, J. C.; Fu, L.; Shan, J.; Mak, K. F. Stripe phases in WSe₂/WS₂ moiré superlattices. *Nat. Mater.* **2021**, *20*, 940–944.
- (16) Cao, Y.; Fatemi, V.; Demir, A.; Fang, S.; Tomarken, S. L.; Luo, J. Y.; Sanchez-Yamagishi, J. D.; Watanabe, K.; Taniguchi, T.; Kaxiras, E.; Ashoori, R. C.; Jarillo-Herrero, P. Correlated insulator behaviour at half-filling in magic-angle graphene superlattices. *Nature* **2018**, *556*, 80–84.
- (17) Cao, Y.; Fatemi, V.; Fang, S.; Watanabe, K.; Taniguchi, T.; Kaxiras, E.; Jarillo-Herrero, P. Unconventional superconductivity in magic-angle graphene superlattices. *Nature* **2018**, *556*, 43–50.
- (18) Sharpe, A. L.; Fox, E. J.; Barnard, A. W.; Finney, J.; Watanabe, K.; Taniguchi, T.; Kastner, M. A.; Goldhaber-Gordon, D. Emergent ferromagnetism near three-quarters filling in twisted bilayer graphene. *Science* **2019**, *365*, 605–608.
- (19) Serlin, M.; Tschirhart, C. L.; Polshyn, H.; Zhang, Y.; Zhu, J.; Watanabe, K.; Taniguchi, T.; Balents, L.; Young, A. F. Intrinsic quantized anomalous Hall effect in a moiré heterostructure. *Science* **2020**, *367*, 900–903.
- (20) Tschirhart, C. L.; Serlin, M.; Polshyn, H.; Shragai, A.; Xia, Z.; Zhu, J.; Zhang, Y.; Watanabe, K.; Taniguchi, T.; Huber, M. E.; Young, A. F. Imaging orbital ferromagnetism in a moiré Chern insulator. *Science* **2021**, *372*, 1323–1327.
- (21) Luttinger, J. M. Fermi surface and some simple equilibrium properties of a system of interacting fermions. *Phys. Rev.* **1960**, *119*, 1153.
- (22) Voit, J. One-dimensional Fermi liquids. *Rep. Prog. Phys.* **1995**, *58*, 977.
- (23) Ishii, H.; Kataura, H.; Shiozawa, H.; Yoshioka, H.; Otsubo, H.; Takayama, Y.; Miyahara, T.; Suzuki, S.; Achiba, Y.; Nakatake, M.; Narimura, T.; Higashiguchi, M.; Shimada, K.; Namatame, H.; Taniguchi, M. Direct observation of Tomonaga-Luttinger-liquid state in carbon nanotubes at low temperatures. *Nature* **2003**, *426*, 540.
- (24) Yao, Z.; Postma, H. W. C.; Balents, L.; Dekker, C. Carbon nanotube intramolecular junctions. *Nature* **1999**, *402*, 273.
- (25) Blumenstein, C.; Schäfer, J.; Mietke, S.; Meyer, S.; Dollinger, A.; Lochner, M.; Cui, X.; Patthey, L.; Matzdorf, R.; Claessen, R. Atomically controlled quantum chains hosting a Tomonaga-Luttinger liquid. *Nat. Phys.* **2011**, *7*, 776.
- (26) Jompol, Y.; Ford, C. J. B.; Griffiths, J. P.; Farrer, I.; Jones, G. A. C.; Anderson, D.; Ritchie, D. A.; Silk, T. W.; Schofield, A. J. Probing spin-charge separation in a Tomonaga-Luttinger liquid. *Science* **2009**, *325*, 597–601.
- (27) Jolie, W.; Murray, C.; Weiß, P. S.; Hall, J.; Portner, F.; Atodiresei, N.; Krasheninnikov, A. V.; Busse, C.; Komsa, H.; Rosch, A.; Michely, T. Tomonaga-Luttinger liquid in a box: electrons confined within MoS₂ mirror-twin boundaries. *Phys. Rev. X* **2019**, *9*, 011055.
- (28) Stühler, R.; Reis, F.; Müller, T.; Helbig, T.; Schwemmer, T.; Thomale, R.; Schäfer, J.; Claessen, R. Tomonaga-Luttinger liquid in the edge channels of a quantum spin Hall insulator. *Nat. Phys.* **2020**, *16*, 47–51.
- (29) Xia, Y.; Wang, B.; Zhang, J.; Jin, Y.; Tian, H.; Ho, W.; Xu, H.; Jin, C.; Xie, M. Quantum confined Tomonaga-Luttinger liquid in Mo₆Se₆ nanowires converted from an epitaxial MoSe₂ monolayer. *Nano Lett.* **2020**, *20*, 2094–2099.
- (30) Ma, Y.; Kolekar, S.; Coy Diaz, H.; Aprojanz, J.; Miccoli, I.; Teegenkamp, C.; Batzill, M. Metallic Twin Grain Boundaries Embedded in MoSe₂ Monolayers Grown by Molecular Beam Epitaxy. *ACS Nano* **2017**, *11*, 5130–5139.
- (31) Pielic, B.; Novko, D.; Rakić, I. S.; Cai, J.; Petrović, M.; Ohmann, R.; Vujičić, N.; Basletić, M.; Busse, C.; Kralj, M. Electronic Structure of Quasi-Freestanding WS₂/MoS₂ Heterostructures. *ACS Appl. Mater. Interfaces* **2021**, *13*, 50552–50563.
- (32) Liu, L.; Yang, H.; Huang, Y.; Song, X.; Zhang, Q.; Huang, Z.; Hou, Y.; Chen, Y.; Xu, Z.; Zhang, T.; Wu, X.; Sun, J.; Huang, Y.; Zheng, F.; Li, X.; Yao, Y.; Gao, H.; Wang, Y. Direct identification of Mott Hubbard band pattern beyond charge density wave superlattice in monolayer 1T-NbSe₂. *Nat. Commun.* **2021**, *12*, 1978.
- (33) Zhang, Q.; Huang, Z.; Hou, Y.; Yuan, P.; Xu, Z.; Yang, H.; Song, X.; Chen, Y.; Yang, H.; Zhang, T.; Liu, L.; Gao, H.; Wang, Y. Tuning molecular superlattice by charge-density-wave patterns in two-dimensional monolayer crystals. *J. Phys. Chem. Lett.* **2021**, *12*, 3545–3551.
- (34) Zhang, Q.; Hou, Y.; Zhang, T.; Xu, Z.; Huang, Z.; Yuan, P.; Jia, L.; Yang, H.; Huang, Y.; Ji, W.; Qiao, J.; Wu, X.; Wang, Y. Visualizing Spatial Evolution of Electron-Correlated Interface in Two-Dimensional Heterostructures. *ACS Nano* **2021**, *15*, 16589–16596.
- (35) Chen, Y.; Liu, L.; Song, X.; Yang, H.; Huang, Z.; Zhang, T.; Yang, H.; Gao, H.; Wang, Y. Twisted charge-density-wave patterns in bilayer 2D crystals and modulated electronic states. *2D Mater.* **2022**, *9*, 014007.
- (36) Choi, J. S.; Kim, J.; Byun, I.; Lee, D. H.; Lee, M. J.; Park, B. H.; Lee, C.; Yoon, D.; Cheong, H.; Lee, K. H.; Son, Y.; Park, J. Y.; Salmeron, M. Friction anisotropy-driven domain imaging on exfoliated monolayer graphene. *Science* **2011**, *333*, 607–610.
- (37) Feng, X.; Kwon, S.; Park, J. Y.; Salmeron, M. Superlubric sliding of graphene nanoflakes on graphene. *ACS Nano* **2013**, *7*, 1718–1724.
- (38) Ribeiro-Palau, R.; Zhang, C.; Watanabe, K.; Taniguchi, T.; Hone, J.; Dean, C. R. Twistable electronics with dynamically rotatable heterostructures. *Science* **2018**, *361*, 690–693.
- (39) Liao, M.; Nicolini, P.; Du, L.; Yuan, J.; Wang, S.; Yu, H.; Tang, J.; Cheng, P.; Watanabe, K.; Taniguchi, T.; Gu, L.; Claerbout, V. E. P.; Silva, A.; Kramer, D.; Polcar, T.; Yang, R.; Shi, D.; Zhang, G. Ultra-low friction and edge-pinning effect in large-lattice-mismatch van der Waals heterostructures. *Nat. Mater.* **2022**, *21*, 47–53.
- (40) Schulz, H. J. Wigner crystal in one dimension. *Phys. Rev. Lett.* **1993**, *71*, 1864–1867.
- (41) Wigner, E. On the interaction of electrons in metals. *Phys. Rev.* **1934**, *46*, 1002–1011.

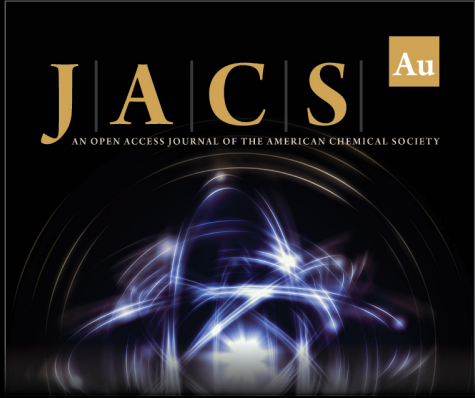
(42) Shapir, I.; Hamo, A.; Pecker, S.; Moca, C. P.; Legeza, Ö.; Zarand, G.; Ilani, S. Imaging the electronic Wigner crystal in one dimension. *Science* **2019**, *364*, 870–875.

(43) Zhou, Y.; Sung, J.; Brutschea, E.; Esterlis, I.; Wang, Y.; Scuri, G.; Gelly, R. J.; Heo, H.; Taniguchi, T.; Watanabe, K.; Zaránd, G.; Lukin, M. D.; Kim, P.; Demler, E.; Park, H. Bilayer Wigner crystals in a transition metal dichalcogenide heterostructure. *Nature* **2021**, *595*, 48–52.


(44) Smolenski, T.; Dolgirev, P. E.; Kuhlenkamp, C.; Popert, A.; Shimazaki, Y.; Back, P.; Lu, X.; Kroner, M.; Watanabe, K.; Taniguchi, T.; Esterlis, I.; Demler, E.; Imamoglu, A. Signatures of Wigner crystal of electrons in a monolayer semiconductor. *Nature* **2021**, *595*, 53–57.


(45) Deshpande, V. V.; Bockrath, M. The one-dimensional Wigner crystal in carbon nanotubes. *Nat. Phys.* **2008**, *4*, 314–318.


(46) Aishwarya, A.; Howard, S.; Padhi, B.; Wang, L.; Cheong, S.; Phillips, P. W.; Madhavan, V. Visualizing 1D zigzag Wigner crystallization at domain walls in the Mott Insulator TaS₂. *arXiv* **2019**, <https://arxiv.org/abs/1906.11983> (accessed June 27, 2019).



JACS Au
AN OPEN ACCESS JOURNAL OF THE AMERICAN CHEMICAL SOCIETY

 Editor-in-Chief
Prof. Christopher W. Jones
Georgia Institute of Technology, USA

Open for Submissions 

pubs.acs.org/jacsau  ACS Publications
Most Trusted. Most Cited. Most Read.